ASTRONOMY & ASTROPHYSICS
SUPPLEMENT SERIES

Astron. Astrophys. Suppl. Ser. **113,** 347-357 (1995)

3D spectrography at high spatial resolution. I. Concept and realisation of the integral field spectrograph TIGER

R. Bacon,[1] G. Adam,[1] A. Baranne,[2] G. Courtès,[2] D. Dubet,[1] J.P. Dubois,[1] E. Emsellem,[1,3] P. Ferruit,[1] Y. Georgelin,[2] G. Monnet,[1] E. Pécontal,[1] A. Rousset[1] and F. Sayède[1]

[1] Centre de Recherche Astronomique de Lyon (UMR CNRS 142 - Ecole Norm. Sup. de Lyon - Univ. Cl. Bernard Lyon I), Observatoire Astronomique de Lyon, 9 Avenue Charles André, 69561 Saint Genis-Laval Cedex, France
[2] Observatoire de Marseille, 2 place Le Verrier, 13248 Marseille Cedex 04, France
[3] Sterrewatcht Leiden, Postbus 9513, 2300 RA Leiden, The Netherlands

Received December 23, 1994; accepted March 28, 1995

Abstract. — The instrument TIGER is the first prototype of an integral field spectrograph using a microlenses array to perform bidimensional high spatial resolution spectrographic observations. It has been in operation at CFHT for a few years and has been successfully used on a large variety of astrophysical objects, ranging from the planet Mars to distant radio-galaxies and quasars. We discuss the fundamentals of the TIGER design and show that it is superior to long-slit spectrography for high spatial resolution purposes. The main characteristics of the instrument are given and some of the astrophysical results are briefly reviewed.

Key words: instrumentation: spectrographes

1. Introduction

The recording of the spectrophotometric information content of a celestial object is, in the general case, a three-dimensional problem (x; y; λ). Unfortunately, however, present detectors are of a two-dimensional nature only and this explains the still prevalent use of classical long-slit spectrographs, despite total loss of one of the spatial coordinates (across the slit width) and because of their perfect geometrical match with available digital detectors.

There are two general classes of solution to this problem: *spectrometers*, for which time scanning is used to provide the missing third dimension, and *integral field spectrographs (IFS)* which manage to cram the full data from a single exposure on the chip. Various examples of the first class, the λ-scanning Fabry-Perot (Taylor & Atherton 1980; Boulesteix et al. 1983) or 2D Fourier transform spectrometers (Maillard 1994) and the y-scanning long-slit grating spectrometer (Wilkinson et al. 1986) are currently used for astronomical work at optical and infrared wavelength.

The first realisation of an IFS was initiated by Vanderriest (1980): it uses optical fibers to transform the bidimensional field into a pseudo slit at the entrance of a classical long-slit spectrograph. A few such fiber-type IFS are in operation around the world: at CFHT with SILFID (Vanderriest 1980) and MOS/ARGUS, and at the Canarias (Garcia-Marin et al. 1994) and Sierra Nevada (Spain) observatories. Another concept, proposed by G. Courtès (1982), uses a microlenses array as a spatial sampler. Both solutions allow retrieval of the tridimensional astronomical information on a 2D detector without the loss of sensitivity and spatial resolution associated with time-scanning schemes. This multiplex property presents many advantages, which makes these concepts particularly suitable for low to medium spectral resolution studies of faint object, combined with a high spatial resolution capability.

The integral field spectrograph TIGER[1] is the first realisation of the Courtès concept. Since its first light at the CFH[2] 3.6 m telescope in 1987, TIGER has undergone few substantial optical and electro-mechanical modifications. It has been operating regularly at CFHT since the end of 1990, and has been used by six different teams on a large

Send offprint requests to: R. Bacon: bacon@obs.univ-lyon1.fr

[1]The prototype was nicknamed TIGER because it has to share the same cage (focal reducer) with PUMA (**PU**nching **MA**chine, the ancestor of the MOS spectrograph). This French acronym stands for "**T**raitement **I**ntégral des **G**alaxies par l'**E**tude de leurs **R**aies".

[2]The Canada-France-Hawaii i Telescope is operated by the National Reasearch Council of Canada, the Centre National de la Recherche Scientifique of France and the University of Hawaii.

variety of objects ranging from the planet Mars to distant radio-galaxies.

The successful first test of the TIGER design originated from the joint effort of R. Bacon, G. Courtès, Y. Georgelin, G. Monnet with the help of G. Lelièvre, executive director of CFHT at that time, who kindly offered some discretionary time. However the realisation of an instrument based on such an original concept is a complex and long lasting undertaking, and its success belongs also to all of those who joined the scientific team or participated in its development and fabrication.

This paper is organized as follows: In Sect. 2, we discuss the limitations of long-slit spectroscopy for high spatial resolution studies. We then give in Sects. 3 and 4 the basics of the optical design. Section 5 briefly presents the mechanical design and Sect. 6 the observational characteristics. Finally in Sect. 7 we discuss some astrophysical applications and Sect. 8 is a brief conclusion. A detailed discussion of the data reduction is given in the companion paper (Rousset et al. 1994, hereafter Paper II).

2. Long slit spectroscopy at high spatial resolution

The primary objective which motivates the design of TIGER (and more generally of IFS techniques) is to fill the gap between the increasing spatial resolution of imaging instruments with the still poor spatial resolution (i.e. $\sim$ 1 arcsec.) and spatial coverage of classical long-slit spectrographic observations.

As shown in this section, reducing the slit width on the sky cannot solve the problem because of the intrinsic difficulties linked to the use of a long-slit. This is a clear limitation for the use of a long slit at high spatial resolution and justifies the development of new IFS capabilities.

2.1. *Light loss and slit effect*

In classical long-slit spectroscopy, the adjustment of the slit width to the seeing disk is always difficult. On the one hand, one would like to minimize the light-loss with a slit width significantly larger than the seeing disk. On the other hand, small displacements of the object with respect to the slit center produce a systematic wavelength error, the slit being asymmetrically illuminated (Fig. 1).

This phenomenon, known as the slit effect, is more critical when the slit width is large compared to the seeing. It can be easily evaluated if we assume a Gaussian function for the seeing disk. Equation (1) gives then the fraction of light intercepted by the slit (K) as a function of the offcentering (d) of the source with respect to the slit center, while Eq. (2) gives the corresponding error (x_0) computed as the displacement on the slit of the output light center,

$$K(f,d) = \frac{1}{\sqrt{2\pi}\sigma} \int_{-0.5f}^{+0.5f} e^{-\frac{(t-d)^2}{2\sigma^2}} dt \qquad (1)$$

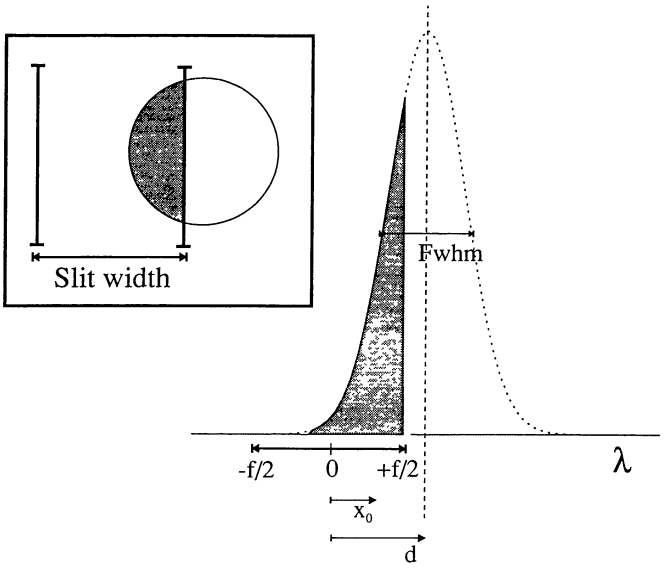

Fig. 1. Slit width effect

$$x_0(f,d) = \frac{1}{K(f,d)} \frac{1}{\sqrt{2\pi}\sigma} \int_{-0.5f}^{+0.5f} e^{-\frac{(t-d)^2}{2\sigma^2}} t dt \qquad (2)$$

σ and f being respectively the seeing and slit width. Of course, x_0 leads directly to a wavelength error, according to the spectral dispersion of the instrument.

Graphs of these two functions are shown in Fig. 2 for two slit widths: a *classical* width of 1.4 FWHM seeing disk and a narrower one of half the FWHM seeing disk. Note that with the larger slit width, even a relative small displacement (20%) of the slit produces a notable error (17% of the slit width) in wavelength. Moreover, the instrumental spectral PSF which is the convolution product of this asymmetric profile with the spectrograph PSF, can be severely affected by this effect, leading to errors in the derivation of line shapes. This error, as well as the loss of light, grows very rapidly with the offcentering of the light source. Thus, being insensitive to slit misplacements requires a narrow slit, but at the expense of keeping only 40% of the total light at best.

One might argue that we can save both light and wavelength accuracy if the object can be precisely centered (better than 10% of the slit width) on the slit. Most modern spectrographs incorporate an imaging capability (using the same detector), which is required to get this centering precision[3]. However broad band images may not be representative of the true geometry of the physical property we are looking for in the object's spectra. There are numerous examples of such mismatches: e.g. the ionized gas (revealed through emission lines) is generally offcentered from continuum emission (seen in broad band images) in Seyfert nuclei (e.g. NGC 5728, Pécontal et al.

[3]This requires however a precision of 0.2 pixel if the slit is 2 pixels width on the detector.

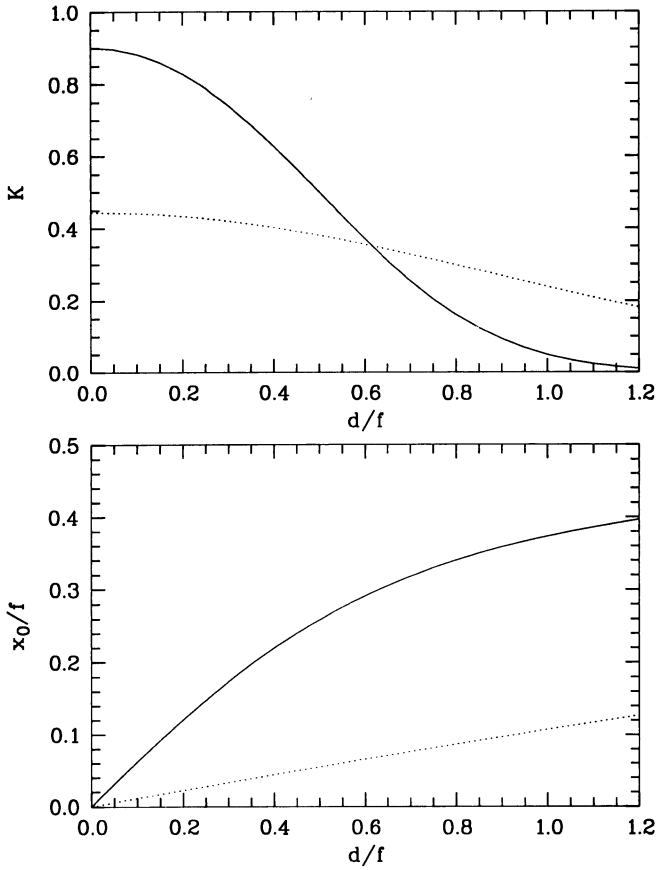

Fig. 2. Estimate of the slit effect for two slit widths: 1.4 times (solid lines) and half (dashed lines) the seeing FWHM. Upper panel: fraction of light intercepted by the slit (K) as a function of the offcentering (d/f) of the source with respect to the slit center. Lower panel: resulting wavelength error (x_0/f) in unit of slit width

1990). If narrow band imaging might solve the problem in this case, there are others circumstances where the physical property of interest cannot be expected to follow the same distribution as the light, whatever the spectral range is: e.g. the kinematical centers in NGC 3227 (gas) and in M 31 (stars) are offset from the maximum of light (Mediavilla & Arribas 1993; Bacon et al. 1994).

2.2. *Object and slit geometry matching*

Besides the error in wavelength, due to a possible misalignement of the slit with respect to the light source, studies made with a long slit generally suffer from a large loss of information due to the object and slit geometry mismatching.

To illustrate this difficulty, we constructed an artificial galaxy (Fig. 3) exhibiting a tilted nuclear disk and a double peaked nucleus structure offcentered from the geometrical center of the galaxy. Progress in spatial resolution imaging shows that such structures are rather common in galaxies: e.g. the nucleus of M31 is tilted by about 10 degrees with respect to the outer bulge and harbours a double peaked structure (Lauer et al. 1993), the "well-known" double nucleus of NGC 6240 when observed at high spatial resolution is resolved into several compact knots with angular sizes of about 0.1−0.2 arcsec (Barbieri et al. 1993), many ellipticals exhibit isophote twists in their central regions, or tilted gas disks revealing their (supposed) triaxial morphology (Goudfrooij et al. 1994), NGC 1068 nucleus, as most of Seyfert ones, presents several hot spots (Evans et al. 1991), etc...

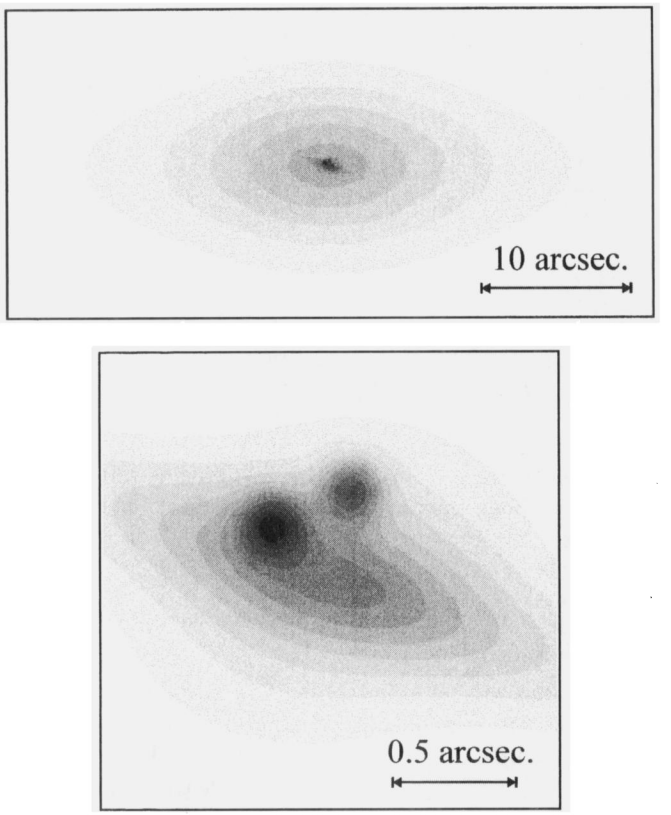

Fig. 3. Artificial galaxy: General view (upper panel) and zoom of the central part (lower panel)

Figure 4 presents the appearance of this artificial object at increasing spatial resolutions, as seen by an IFS with a spatial sampling (40×40 elements) equal to half the resolution. The corresponding long slit light profile is given for comparison.

At low spatial resolution (2 arcsec) the galaxy appears quite symmetrical. Two long slit exposures along the major and minor photometric axes, will then give most of the spectrographic information. Note that the long slit used with the same detector (2048^2 pixels) is much longer (11 arcmin) than the IFS linear size (40 arcsec). For this relatively compact object, IFS is nevertheless more efficient than the long slit, because it gives roughly the same result in half the telescope time. Moreover, seeing and sky transparency may change from one long slit exposure to

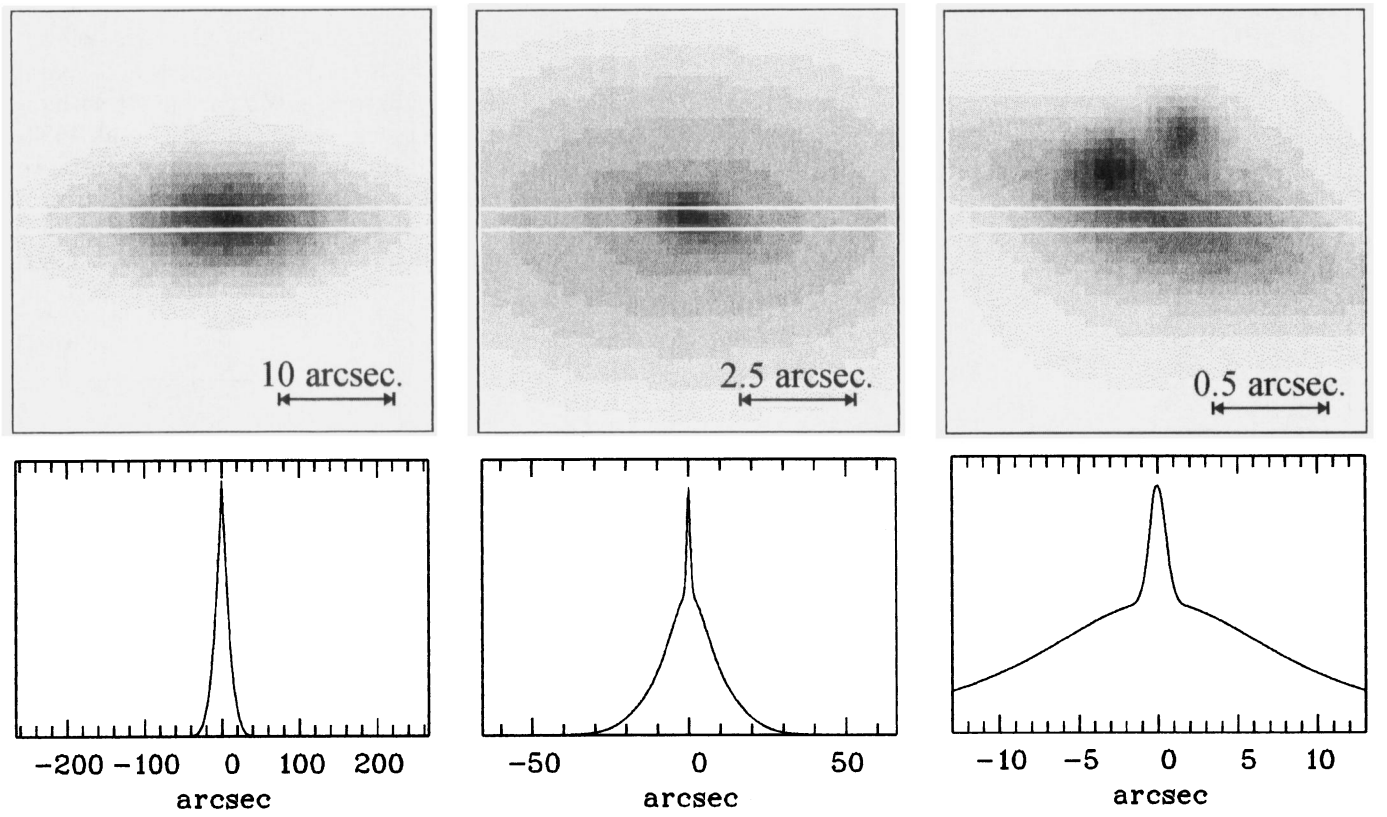

Fig. 4. Aspect of an artificial galaxy observed with IFS and long slit techniques at increasing spatial resolution. Top: IFS image, bottom: cut along the slit. The spatial resolution is respectively 2 (left), 0.5 (center) and 0.1 (right) arcsec FWHM. The white solid lines shows the corresponding slit location on the IFS images

another, possibly leading to errors when comparing major and minor axis data.

At higher spatial resolution (0.5 arcsec), the galaxy is still roughly symmetrical, but the tilted nuclear disk becomes slightly visible. Except if the user has already a high resolution image *and* if the disk clearly stands out[4], he/she will choose a *wrong* orientation for the slit. Central velocity profiles derived from the major and minor axis exposures can then be easily *misinterpreted*. On the other hand, the galaxy covers almost completely the field of view in the IFS exposure, so that spectrographic information in the faint outer part could be difficult to extract because of uncertainties in sky subtraction. This problem does not occur with the long slit exposures because of their much larger linear size.

At the highest spatial resolution (0.1 arcsec), the object is far from being symmetrical. A long slit exposure, if aligned with the photometric major axis of the galaxy, *would completely miss the nuclear structures*. Moreover, the bright peak being located just at the edge of the slit, *would distort the spectral properties* because of the slit effect.

This example highlights the intrinsic difficulties met when using a long slit at high spatial resolution. More generally, it shows that the choice of a location for the slit is already a strong a priori assumption about the object properties that one is endeavouring to measure.

3. TIGER optical design

The solution to most of the problems occurring in slit techniques, is an IFS design where the spatial and spectral properties are uncorrelated. In addition, this design should allow simultaneous acquisition of spatial and spectral information in order to avoid the difficulties of varying atmosphere transmission and seeing encountered for the scanning schemes.

As we will see, the Courtès concept of IFS with a microlenses array matches these requirements. The schematic layout of the optical configuration is illustrated in Fig. 5. The field of view (image A in Fig. 5) is enlarged and focused on the microlenses array by an objective and a field lens. The array performs the spatial sampling (image B in Fig. 5). Each microlens produces an image of the exit pupil (image C in Fig. 5) whose size is much smaller

[4]This might not be the case if, for example, the nuclear disk appears only as a second component in the velocity profile of the galaxy.

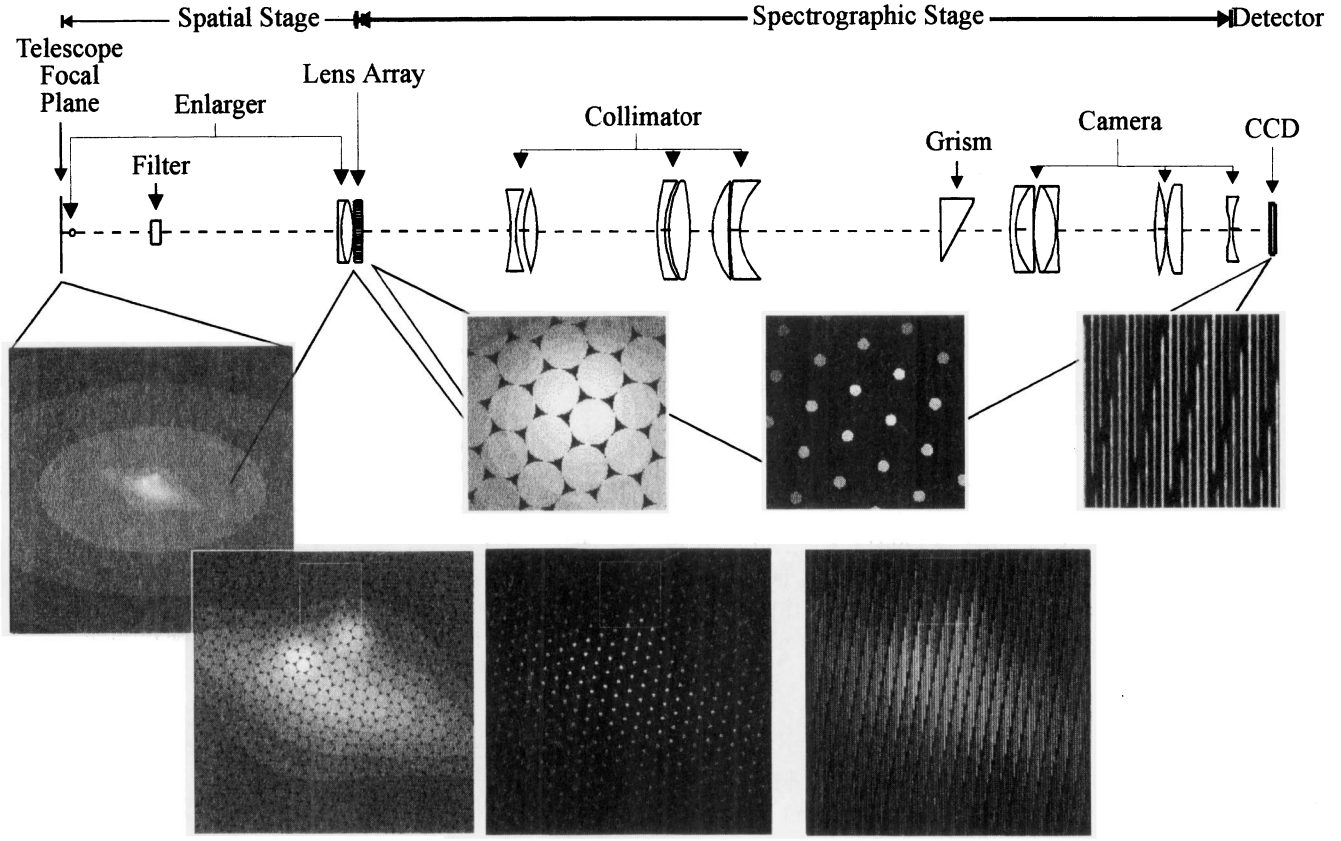

Fig. 5. TIGER optical design.

($\sim$ 45 μm) than the input lens diameter (1.4 mm). The remaining part is a classical grism-based spectrograph. Each micropupil, dispersed by the grism, providing a spectrum on the CCD (image D in Fig. 5). A slight rotation between the dispersion axis and the microlenses array, combined with the use of a wide band interference filter, avoids spectra overlapping. Note that, in contrast to the ARGUS design, where a fibers bundle is used to re-arrange spectra on a pseudo-slit, only classical refractive optics is used in the TIGER design. This has a few advantages, as the conservation of the aperture ratio and the possibility to have a complete sampling (hexagonal or square lenses) without light-loss. However, as it will be seen later, the two designs are quite complementary.

Some important features of the TIGER design are listed below:

- The efficiency of the geometrical spatial coverage with circular microlenses array is 91% and can theoretically reached 100% with hexagonal or square lenses. This is to be compared with the ~70% of fiber bundles due to their cladding.
- In contrast to classical spectrographs, the pupil rather than the field is imaged on the detector. This allows the spectrographic point spread function to be independent of the spatial content of the field.
- Each spectrum is well separated ($\sim$ 7 pixels) from its neighbours. This ensures that optical aberrations of the spectrograph will not degrade at all the spatial resolution.
- A drawback of this field-pupil inversion is the need for accurate alignment between sky and calibration pupils. Indeed any misalignement of these pupils would lead to wavelength calibration errors, as the reference spectra would be shifted with respect to the object ones. This effect has been minimized in TIGER with a slit, oriented perpendicular to the dispersion direction, which masks the pupil located just at the output of the enlarger. This costs 10% of the light, but on the other hand gives a sharper PSF in the wavelength direction.
- As for any classical multi-slit spectrographs, some spectra are truncated at the edge of the detector. It follows that the spectral length in pixel must be limited to a fraction of the detector linear size in order to avoid too large a fraction of truncated spectra.
- Microlenses have a better transmission ($\sim$ 96%) than fibers, especially in the near UV[5].
- Optimal sampling is attained when the microlens size is less than half the seeing disk. Undersampling can affect the pupil illumination and is not recommended.

[5]Far UV space astronomy is possible using a micromirror array as proposed by Courtès et al. (1985).

4. Optimisation of the optical parameters

In this section we detail the practical optimisation of the various optical parameters involved in the TIGER design.

4.1. *The detector*

Obviously the detector should have the largest possible format and a high quantum efficiency. Single CCDs can now reach quantum efficiencies up to 90% and rather respectable formats (2048^2 pixels). In the remaining part of this paper we will use as an example a detector with 2048×2048 15 μm pixels.

4.2. *The microlenses array format*

According to Sect. 3, the number of spatial elements ($n_{\rm L}$) is the number of microlenses whose exit pupil is imaged on the detector. It is simply related to the total area of the CCD and the area of an individual spectrum:

$$n_{\rm L} = \frac{n_x n_y}{\delta_x l_{\rm S}} \tag{3}$$

with n_x, n_y beeing the CCD x and y format, $l_{\rm S}$ and δ_x respectively the spectral length and the separation between two adjacent spectra, in pixels[6]. δ_x should be minimized in order to maximise the number of spectra for a given spectrum length, but obviously cannot be less than a few pixels.

4.2.1. Separation between two adjacent spectra

In this design, as opposed to long-slit spectrographs, two adjacent spectra on the CCD do not necessarily originate from adjacent spatial elements. Indeed, neighbouring spectra are shifted by $d_{\rm Lcos}(\alpha)$ pixels along the y axis, $d_{\rm L}$ being the microlens diameter in pixels and α the (small) rotation of the microlenses array with respect to the y axis. It follows that the measured intensities of two neighbouring spectra, taken along the same CCD line, do not originate from the same wavelength. It is thus necessary to avoid any overlapping in the cross-dispersion direction, even if adjacent spectra are spatial neighbours. This, together with the cross-dispersion profile, sets the value of δ_x.

We will now compute an estimate of this spectral cross-talk. In the following we will assume a Gaussian shape for the cross-dispersion profile P_x:

$$P_x = \frac{A_0}{\sqrt{2\pi}\sigma_x} \exp\left\{-\frac{(x-x_0)^2}{2\sigma_x^2}\right\} \tag{4}$$

For simplicity, σ_x is supposed to be constant over the whole spectral range.

[6] In this paper, we define the y axis as the dispersion axis.

The true intensity A_0 at a given wavelength is simply the area of the cross-dispersion profile and can in principle be recovered by global summation over line pixels. In practice we stop the summation at a given width (w), and we miss some flux. The relative loss is then.

$$\frac{\Delta_f A}{A_0}(w) = 1 - \int_{-w}^{+w} \frac{1}{\sqrt{2\pi}\sigma_x} \exp\left\{-\frac{x^2}{2\sigma_x^2}\right\} {\rm d}x \tag{5}$$

It is thus advantageous to sum cross-dispersion intensities over a large window, but this increases the cross-talk $\Delta_p A$ between neighbouring spectra, with:

$$\frac{\Delta_p A}{A_0}(w) = \frac{A_{+1}}{A_0} \int_{-w}^{+w} \frac{1}{\sqrt{2\pi}\sigma_x} \exp\left\{-\frac{(x-\delta_x)^2}{2\sigma_x^2}\right\} {\rm d}x + \frac{A_{-1}}{A_0} \int_{-w}^{+w} \frac{1}{\sqrt{2\pi}\sigma_x} \exp\left\{-\frac{(x+\delta_x)^2}{2\sigma_x^2}\right\} {\rm d}x \tag{6}$$

A_{+1} and A_{-1} being respectively the total intensity of the right and left cross-dispersion profiles.

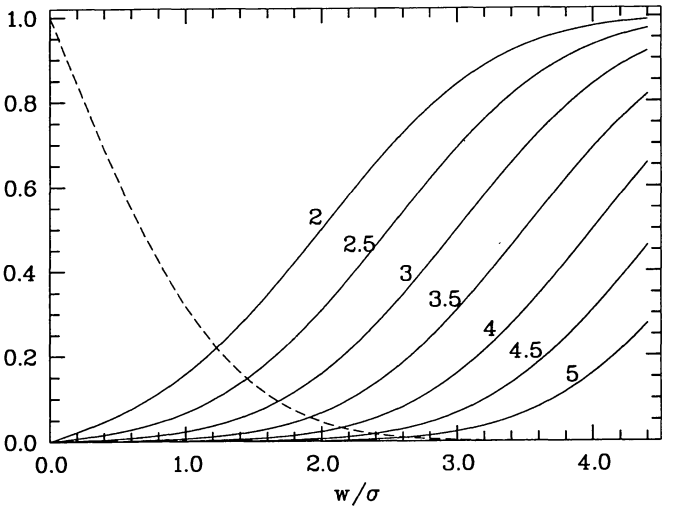

Fig. 6. Estimate of truncation versus cross-talk errors according to the summation half width w/σ_x. Truncation error (dashed line): $\Delta_f A/A_0$. Cross-talk error (solid lines) on one side: $\Delta_p A/A_{+1}$ or $\Delta_p A/A_{-1}$. Curves are labelled according to the value of the δ_x/σ_x parameter

Figure 6 shows the competition between these two errors as functions of the width summation (w) for various values of the δ_x/σ_x parameter. It shows that we should severely limit the summation window to avoid unreasonable cross-talk errors in the case of small δ_x/σ_x, but this would increase the truncation error to unacceptable value. On the other hand, a large value of this parameter would give satisfactory results in term of both types of errors but will reduce the total number of spectra according to Eq. (3). A value of $\delta_x/\sigma_x \sim 3.5$ is a good compromise: summing over $\pm 1.7\sigma_x$ pixels allows us to retrieve up to 90% of the total flux and the cross-talk is limited to $3.5A_{\pm 1}/A_0$%.

However in an unfavourable case with $A_{\pm1}/A_0 \sim 100$ (e.g. a strong emission line rising over a faint continuum) we should limit the summation window to $\pm 1.2\sigma_x$ to keep the cross-talk to 1%, but the truncation loss is increased to 23%. This computation shows also that we should limit the width of the cross-dispersion (σ_x) to the minimum required to get a correct spectral sampling (i.e. ~ 2 pixels).

We have seen that the peculiar hexagonal arrangement of spectra in the TIGER design could introduce errors in the retrieved flux due to cross-talk between individual spectra. This may look like a severe limitation of this design. However, we have shown that these errors can be limited to reasonable values with a proper spectra separation.

It will be demonstrated in Paper II that a major improvement is possible when taking into account the true shape of the cross-dispersion profile which is a priori known. This leads to a virtually *loss-free* extraction of the physical information.

4.2.2. Spectral length

The spectral length in pixels (l_S) is a free parameter which may range from 1 to n_y. However the hexagonal arrangement introduces a truncation of some spectra by the detector edges. The fraction of truncated spectra F_T is simply:

$$F_T = \frac{l_S}{n_y} \tag{7}$$

In order to get a large enough useful spatial field, we should limit F_T to a reasonable value, say 20%. Practically the spectral length in Angstroem is fixed by the grism, the focal length of the camera and the broad band interference filter. The latter cannot have a perfectly rectangular transmission curve and, consequently, the useful spectral length[7] (l'_S) is smaller than its total length (l_S). Good interference filters have roughly $l'_s \sim 0.8 l_S$. Using the upper limit of 20% for F_T, we get:

$$F_T = \frac{l'_S}{n_y} \leq 0.2 \tag{8}$$

which gives finally $l_S \leq 0.25\ n_y$. Using Eq. (3) we get the corresponding minimum number of microlenses allowed to get a compact storage on the detector while keeping the number of truncated spectra small enough:

$$n_L \geq \frac{n_x}{0.25\delta_x} \tag{9}$$

which gives $n_L \geq 0.57 n_x$ if we adopt a value of 7 for δ_x, as has been suggested in the last section.

[7]It may be defined for instance as the wavelength range where the filter transmission is greater than 50% of its maximum transmission.

From the number of possible configurations[8] for a 2048^2 CCD, the one which maximises the spectral coverage will have 512 spectral (412 useful) and 1167 spatial elements. On the other hand, there is a practical lower limit for the spectral range. For instance, we need a minimum spectral range to fit the continuum above the emission lines. Taking 100 spectral (80 useful) elements as lower limit, we get a maximum of 5992 spatial elements for our 2k CCD. It turns out that the TIGER design favours spatial versus spectral coverage and, in that respect, is complementary to the optical fiber ARGUS design which has a larger spectral range, but a smaller spatial field[9].

4.2.3. Microlens diameter

The separation between the microlens pupil images on the detector (Δ'_L) could easily be derived using the hexagonal compact pattern geometry:

$$\Delta'_L = \Delta_{pix}\sqrt{\frac{2}{\sqrt{3}}\delta_x l_S} \tag{10}$$

Δ_{pix} being the detector pixel size.

The true microlens size Δ_L is $\gamma_e \Delta'_L$, where γ_e is the magnification of the focal reducer. Using the lower (100) and upper (512) spectral length limits, we get the corresponding limits on the microlens diameter (with a 2k CCD):

$$0.4 < \gamma_e \Delta_L(\text{mm}) < 1.0 \tag{11}$$

We will see in the next section that the aperture ratio of the camera is generally large (e.g. $f/4$); this sets a lower limit on the focal reducer magnification to get a manageable collimator aperture ratio. Taking $\gamma_e < 2$ gives 0.2 mm as the lowest lens diameter.

4.3. *The spectral stage*

4.3.1. The camera

The spatial sampling in arcsec. (i.e. the size of a microlens on the sky) is related to the size of a micropupil through the beam extent conservation between the telescope primary mirror and the detector plane. It gives:

$$\theta_{sky} D_{tel} = O_{cam} d_{pup} \tag{12}$$

where θ_{sky}, O_{cam}, D_{tel}, d_{pup} are respectively the spatial sampling, the camera aperture, the telescope primary mirror diameter and the micropupil size on the detector. This latter is closely related to the spectral resolution, as the true monochromatic image is its convolution product with the point spread function (PSF) of the focal reducer. In

[8]The final choice of one configuration will depend on the observing program.

[9]ARGUS design for a 2k CCD would have 2048 spectral elements and $\sim$ 500 spatial elements.

the previous section we found that the width of the cross-dispersion profile is critical and should be ~ 2 pixels. However, development and fabrication of optics offering low aberrations and distortions over a large field together with high transmission is a difficult task. Thus a focal reducer with a PSF ≤ 2 pixels over the whole field would be acceptable. Assuming that both PSF and micropupil image have a gaussian shape[10], the cross-dispersion profile width is then:

$$\sigma_x = \sqrt{d_{\rm pup}^2 + {\rm PSF}^2} \tag{13}$$

To get $\sigma_x < 2.5$ pixels we must have $d_{\rm pup} < 1.5$ pixels keeping PSF ~ 2 pixels. This corresponds to an upper limit of the spatial sampling for a given aperture ratio of the camera (using Eq. 12):

$$\theta_{\rm sky} < \frac{1.5\, O_{\rm cam} \Delta_{\rm pix}}{D_{\rm tel}} \tag{14}$$

We must then find a compromise between the largest spatial sampling (with a correspondingly larger field of view) and the camera opening ratio which is limited by CCD flatness and reflections to $\leq f/2$. Using this value, we get 0.6 arcsec maximum spatial sampling for a 3.6 m telescope and a 15 μm pixel CCD. This parameter is 1.2 arcsec and 0.30 arcsec respectively for a 2 m and a 8 m telescope[11]. On the other hand there is no lower limit for the spatial sampling since the micropupil width becomes rapidly negligible compared to the focal reducer PSF (this ensures that the Shannon criterion will always be satisfied if PSF ~ 2 pixels).

4.3.2. The dispersor

The dispersion is limited at the higher end by the grating or grism angular dispersion and the focal length of the camera. Today's technology gives a practical limit of 600 and 1200 g.mm^{-1} for respectively refracting and reflecting gratings. On the other hand the camera focal length is restricted by its entrance pupil size (Ω), the f-ratio of the camera being set by the spatial sampling as shown in the previous section.

At the lower end, the dispersion is limited by the intrusion of strong zeroth order on the detector. As grating spectrographs give a nearly linear dispersion, the interval Δ_{01} between the zero and first order is related to the spectral PSF width (P_y) by;

$$\frac{\Delta_{01}}{P_y} \sim \frac{\lambda_0}{\Delta\lambda} = R \tag{15}$$

[10]This is not true for the micropupil image which is the exact image of the primary mirror including the central obscuration.
[11]This value may be too small, except for an adaptive optics corrected focus. To get a larger value one must used a detector with larger pixels.

Obviously Δ_{01} should be smaller than the detector size (n_y), which yields a lower limit for the resolving power of:

$$R > \frac{n_y}{{\rm PSF}_y} \tag{16}$$

For example, we get a spectral resolution range of 1000-2600 at 6500 Å with a $2048^2 \times 15$ μm pixel CCD, a 2 pixel P_y and a 200 mm camera focal length. With larger CCDs (e.g. 4096^2), this problem becomes even more critical ($R > 2000$). In the blue wavelength range, a prism can be used to overcome this limitation. However, for low dispersion studies, the ARGUS design should be preferred at the expense of fewer spatial elements.

4.3.3. The focal reducer magnification

The remaining free parameter is the focal reducer magnification ($\gamma_{\rm e}$) which is by definition:

$$\gamma_{\rm e} = \frac{O_{\rm coll}}{O_{\rm cam}} = \frac{f_{\rm cam}}{f_{\rm coll}} \tag{17}$$

$O_{\rm coll}$ and $O_{\rm cam}$ being respectively the collimator and camera apertures.

We have seen in Sect. 4.3.1 that we should have a large aperture for the camera (e.g. $f/4$) to get a reasonable lower limit for the spatial sampling. Using $f/2$ as the upper limit for the collimator aperture, we get $\gamma_{\rm e} < 2$. Then, using Eq. (11) and today's technological limits for the microlenses ($0.1 < \Delta_{\rm L}({\rm mm}) < 2$), we end up with the following range:

$$0.2 < \gamma_{\rm e} < 2 \tag{18}$$

Once $\gamma_{\rm e}$ has been chosen, parameters for the collimator and the microlenses are easily derived. Equation (17) gives the collimator aperture and its focal length. Given Eq. (10) and using the number of spectral elements previously chosen, one can compute the lens diameters, and then the focal length using the fact that their opening ratio is at least equal to the collimator's one.

4.4. *The spatial stage*

The spatial stage, circumvented by the telescope focal plane and the input face of the microlenses, is simply composed of a set of enlargers and field lenses in front of the microlenses array.

The enlarger magnification is given by:

$$\gamma_{\rm a} = \frac{\Delta_{\rm L}}{\theta_{\rm sky}} \tag{19}$$

$\theta_{\rm sky}$ being the spatial sampling size on the sky.

Any spatial sampling can be accommodated provided it is less than the maximum value defined in Sect. 4.3.1, Eq. (14).

5. Mechanical design

The TIGER modules (filter wheel, enlarger wheel, microlenses array/field lens, grism wheel, etc) are mounted on separate plates in a preexisting tubular mechanical structure. These plates can be easily moved along the optical axis. This flexibility has been used to optimize the TIGER configuration in the early phases of development of the instrument.

The switch between spectrographic and imaging modes is easily performed through the rotation of three independent wheels (enlarger, microlenses array/field lens, grism in/out). Their mechanical design has been optimized to ensure the very precise positioning required by TIGER operations.

6. Optical and observational characteristics

TIGER spatial characteristics have been chosen to match the current spatial resolution at CFHT, namely 0.7 arcsec FWHM 70% of the time.

Table 1. TIGER optical characteristics

Wavelength range	0.35–1 μm
Imagery enlarger focal length	40 mm
Imagery enlarger aperture ratio	$f/42$
Spectrographic enlarger 1 focal length	10 mm
Spectrographic enlarger 1 aperture ratio	$f/206$
Spectrographic enlarger 2 focal length	15 mm
Spectrographic enlarger 2 aperture ratio	$f/132$
Micro-lenses array	572 lenses
Micro-lenses diameter	1.39 mm
Micro-lenses focal length	11.4 mm
Micro-lenses aperture ratio	$f/8.2$
Collimator focal length	194 mm
Collimator aperture ratio	$f/8.2$
Grism	150–600 groves
Camera focal length	138 mm
Camera aperture ratio	$f/5.8$
CCD	$1024^2 \times 18$ μm
Total transmission	0.12

Its optical parameters have been optimized for the CFHT SAIC CCD chip of $1024^2 \times 18$ μm pixels. The optical computation of the spectrograph (collimator + camera) has been performed by A. Baranne and subcontracted to the French company CERCO. The microlenses array (Fig. 7) has been realised by the French compagny OFR. Table 1 gives the general optical characteristics, while Table 2 gives the corresponding observational parameters.

7. Astrophysical applications

Because of its small field of view (7×7 and 10×10 arcsec^2), this instrument is clearly optimized for the study of compact structured objects with complex photometric and/or physical properties. This includes a wide variety of scientific targets from the geology of telluric planets to the environment of quasars and encompasses both quiet and active galactic nuclei as prime objectives.

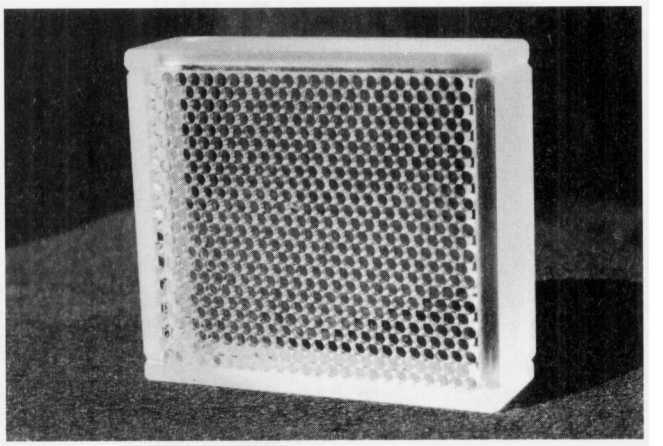

Fig. 7. TIGER microlenses array

Table 2. TIGER observational characteristics. Only a few from the large number of possible spectral configurations are given

Mode	Spatial sampling	Field of view
Imaging	0.16 arcsec	40 × 40 arcsec^2
Spectrographic	0.39 arcsec	7 × 7 arcsec^2
Spectrographic	0.61 arcsec	10 × 10 arcsec^2
Spectral resolution	**Central wavelength**	**Wavelength range**
1300	5010 Å	540 Å
1400	5330 Å	540 Å
1800	6850 Å	540 Å
370	6320 Å	2400 Å
540	7575 Å	2400 Å

Indeed, TIGER has already produced a number of important scientific results; some of them are briefly presented below[12]:

– **Geology of Mars** (Martin et al. 1994): TIGER observations at high spatial resolution (250–300 km) were obtained on the Tharsis dome region, including the transition zone toward the southern dark terrains in Mare Sirenum. These data (~1000 spectra) were used to assess the variability of the Martian surface in the 0.8–1.1 μm domain where spectral variations are strongly dependent on the surface mineralogy. The results show a progressive modification of the spectra morphology at the transition zone crossing, consistent

[12]The reader should refer to the original papers for the scientific results discussed here.

with a relative variable contribution of Fe^{2+} and Fe^{3+} absorption features in the mineralogic properties of the studied area.

- **Nuclei of galaxies** (Bacon et al. 1994; Emsellem et al. 1994): Bidimensional stellar velocity and velocity dispersion fields have been obtained for the first time in the inner 5−10 arcsec diameter of central regions of a few nearby galaxies. In M 31 these data, coupled with high spatial resolution images, show definite subarcsec. offsets between the light maximum, the kinematical center and the peak of the velocity dispersion. In M 104, the highly complex population distribution has been broken down into various components (nucleus, inner and outer disk, bulge). It has, in particular, revealed a new anisotropic disky nuclear component.
- **Seyfert nuclei** (Pécontal et al. 1990, 1994): TIGER has been used to observe a few nearby Seyfert galaxies to study the impact of nuclear activity on galaxies. In NGC 5929, the two emission-line counterparts of the radio lobes have been kinematically disentangled, which allows the mapping of the line ratios and of the velocity fields for each lobe. In M 51 the narrow line emission region is dominated by the extra-nuclear cloud. Velocity slices through the [NII] line display a complex behavior of the emission which is split into various component.
- **Emission-line galaxies** (Ferruit & Pécontal 1994): TIGER observations of the central galaxy of the Perseus cluster NGC 1275 allows to distinguish and map different sources of continuum and emission lines: the nucleus BLR and NLR, the extended emission-line system and the southest part of the infalling galaxy. The main result is the discovery of double-peaked or asymmetric emission lines in the vicinity of most of the brightest clusters observed with HST, which suggests that gas clouds associated with these objects have been detected.
- **Evolution of radiogalaxies** (Rocca-Volmerange et al. 1994): Observation of the z=0.47 radio-galaxy 3C 435A have revealed a remarkable superimposition between the 1.4 Ghz radio lobe and the [OII] and [OIII] emission lines. For the first time, stellar and nebular components are separated at a large redshift, indicating that the alignement effect is mainly due to nebular emission.
- **Ionized gas around quasars** (Durret et al. 1994): Observations of three moderate redshift quasars (TON 616, 4C 37.43 and PKS 2251+113) have shown that the ionized gas in at least two of these objects is very clumpily distributed and shows chaotic velocity fields that cannot be simply accounted for by a single rotating disk. This suggests that interactions must play an important role in the ionized nebulosities surrounding quasars. The ionized blobs are compatible with galaxies interacting with the main envelopes surrounding the quasars.
- **Gravitational lenses** (Adam et al. 1989; Fitte & Adam 1994): Early observation of the Einstein cross (2237+0305) have provided the decisive proof that the four components are multiple images of the same quasar. More recent observations together with published litterature have revealed the history of the microamplifications of its components and have been used to extract the underlying galaxy.

8. Conclusions and prospects

The TIGER prototype developed by the Observatoire de Lyon and Marseille has been successfully used at CFHT during nine runs by six different teams. Together with optical and electro-mechanical optimisation, a major effort has been put in the development and realisation of the data reduction package (see Paper II).

Although it was primarily developed to validate the lenslet IFS concept, it has provided a number of scientific results on a large variety of astrophysical objects. Two other TIGER-type instruments are currently in operation or development: at the Zelenchuk 6 m (Afanasiev 1994) and at the Okayama 1.88 m (Ohtani et al. 1994) telescopes.

With the development of adaptive optics corrected focus, the need for high spatial resolution spectrographic capabilities will grow rapidly. As shown in Sect. 2, slit-spectrographs are inadequate for this specific use whereas TIGER-type IFS fulfill most of the requirements of the images delivered by adaptive optics (i.e. high spatial sampling, small field of view, flexibility to adapt the changing seeing conditions, spectral PSF uncorrelated with object spatial property, no pre-requisite regarding the object geometry). The spectrograph OASIS[13], being built by the Observatoire de Lyon, is a multi-mode integral field spectrograph dedicated to the CFHT adaptive optics bonnette under construction (Arsenault et al. 1994). This instrument features six observing modes including a TIGER one. With a spatial sampling down to 0.05 arcsec and 1400 spectra obtained in one "shot", it will offer new spectrographic capabilities still unmatched, even by those of the Hubble space telescope.

References

Adam G., Bacon R., Courtès G., Georgelin Y., Monnet G., Pécontal E. 1989, A&A 208, L15

Afanasiev V.L. 1995, in Tridimensional optical spectroscopic methods in astrophysics: IAU colloq. 149, ed. G. Comte and M. Marcellin, ASP Conf. Ser. 71, 278

Arribas S., Mediavilla E., Rasilla J.L. 1991, ApJ 369, 260

Arsenault R., Salmon D., Kerr J. et al. 1994, in: S.P.I.E Conf. Inst. Astr., in press

[13] **O**ptically **A**daptive **S**ystem for **I**maging **S**pectrography.

Bacon R., Emsellem E., Monnet G., Nieto J.L. 1994, A&A 281, 691
Barbieri C., Rafanelli P., Schulz H. et al. 1993, A&A 273, 1
Boulesteix J., Georgelin Y., Marcelin M., Monnet G. 1983, in: S.P.I.E. Conf. Inst. Astr. V, 445
Courtès G. 1982, in: Instrumentation for Astronomy with Large Optical Telescopes, ed. C.M. Humphries (Reidel) 123
Courtès G., Donas J., Mauron N., Vanderriest C., Schneider J. 1985, in: LAS-MATRA, HST Faint Object Camera, Second Generation Instrument, doc. AO.OSSA.4.84, pp. 1-110
Durret F., Pécontal E., Petitjean P., Bergeron J. 1994, A&A 291, 392
Emsellem E., Bacon R., Monnet G. 1995, in: Tridimensional optical spectroscopic methods in astrophysics: IAU colloq. 149, eds. G. Comte and M. Marcellin, ASP Conf. Ser. 71, 282
Evans I.N., Kinney A.L., Ford H.C., Antonucci R.R.J., Armus L., Caganoff S. 1991, ApJ 369, L27
Ferruit P., Pécontal E. 1994, A&A 288, 65
Fitte C., Adam G. 1994, A&A 282, 11
Goudfrooij P., Hansen L., Jorgensen H.E. and Norgaard-Nielsen H.U. 1994, A&AS 105, 341
Hes R., Peletier R.F. 1992, A&A 268, 539
Lauer T.R., Faber S.M., Groth E.J. et al. 1993, AJ 106, 1436
Mediavilla E., Arribas S. 1993, Nature 365, 420
Maillard J.P. 1995, in: Tridimensional optical spectroscopic methods in astrophysics: IAU colloq. 149, eds. G. Comte and M. Marcellin 1995, ASP Conf. Ser. 71, 316
Martin P., Pinet P., Bacon R., Rousset A. 1995, in: Tridimensional optical spectroscopic methods in astrophysics: IAU colloq. 149, eds. G. Comte and M. Marcellin M., ASP Conf. Ser. 71, 298
Ohtani H., Sasaki M., Aoki K., Takano E., Kiyohara M. 1994, in: S.P.I.E Conf. Inst. Astr., in press
Pécontal E., Adam G., Bacon R., Courtès G., Georgelin Y., Monnet G. 1990, A&A 232, 331
Pécontal E., Ferruit P., Wilson A.S. 1995, in: Tridimensional optical spectroscopic methods in astrophysics: IAU colloq. 149, eds. G. Comte and M. Marcellin, ASP Conf. Ser. 71, 274
Rocca-Volmerange B., Adam G., Ferruit P., Bacon R. 1994, A&A 292, 20
Taylor K., Atherton P. 1980, MNRAS 191, 675
Vanderriest C. 1980, PASP 92, 858
Wilkinson A., Sharples R.H., Fosbury R.A.E., Wallace P.T. 1986, MNRAS 218, 297